JOURNAL OF MATERIALS SCIENCE 29 (1994) 1471–1480

Age-hardening kinetics and microstructure of PH 15-5 stainless steel after laser melting and solution treating

K. OZBAYSAL, O. T. INAL
Materials and Metallurgical Engineering Department, New Mexico Institute of Mining and Technology, Socorro, NM 87801, USA

Microstructural characterization and the kinetics of ageing of 15 PH stainless steel is studied in the fusion zone and in solution-treated and quenched (as-quenched) samples. Fusion zone had a finer structure than the as-quenched samples due to melting and subsequent solidification. This had a major effect on the amount of the hardness received in the fusion zone. The ageing structure of both samples was essentially the same, except for the smaller solidification cell size of the fusion zone. Strengthening was achieved by the formation of coherent precipitation of copper in the b c c martensite. Copper precipitates were found to be related to the parent martensite with a Kurdjumov–Sachs orientation relationship in both samples. Precipitates were spherical in shape and they nucleate and grow both on the dislocations and in the matrix. No incubation period was observed in the hardening curves. Kinetics of precipitation was studied from an Arrhenius type equation for both samples. It was found that, at high ageing temperatures, the activation energy for precipitation hardening was approximately the same as that of the activation energy for substitutional diffusion in b c c ferrite. At lower ageing temperatures, the calculated activation energy was consistent with the activation energy for short circuit diffusion of substitutionals in b c c structure. Microstructural characterization and the activation energy calculations showed that precipitation of copper in both samples was controlled by the diffusion of copper in b c c martensite. At high ageing temperatures, mass transport of copper was through the lattice. At low temperatures, the contribution of high dislocation density to the apparent diffusivity was large.

1. Introduction

In the last decade, lasers have found extensive applications in metallurgy and material science. Their major use in metallurgy involves welding, followed by laser surface modification (either by melting or heat treating to obtain martensite) and laser surface alloying. Depending on the sample scan velocity and the heat input, cooling rate may be varied in the molten zone. As the cooling rate increases, dendritic structure and the size of the solidification grains become finer. At the highest cooling rate, depending on the thermodynamics of the alloy system, a massive transformation may become possible, producing a surface alloy with the same composition of the liquid from which it forms, without any segregation at the cell or solidification boundaries. Therefore, processing of metallic materials with lasers can be called a rapid solidification technique, depending on the processing parameters used which may eventually produce a high cooling rate at the surface if properly designed. Accordingly, highly supersaturated structures can be achieved after melting and solidification at the surface which, through increasing driving force for nucleation and growth, may increase the kinetics of ageing in precipitation hardening systems.

Precipitation of intermetallic compounds in a martensitic matrix is known as an effective method of producing low-carbon, high-strength and high-ductility marage steels. However, marage steels suffer from a low resistance to corrosion and accordingly several marage steels were developed with additions of 13%–17% chromium to increase corrosion resistance [1].

PH stainless steels can be either austenitic, semi-austenitic or martensitic depending on the alloying element additions to the composition. Martensitic PH stainless steels usually contain 4%–7% nickel to keep the M_s temperature above room temperature. Elements added to form precipitates are copper, molybdenum, aluminium, titanium and niobium [2]. The alloys are solution treated, quenched and aged at temperatures between 400 and 500 °C. The precipitation-hardening agents are copper, Ni_3Ti, Ni_3Al and NiAl [3].

Several studies have been reported in the literature generally concerning the microstructural characterization and mechanical behaviour of PH stainless and marage steels. Among the PH stainless steels, 17-4 PH grade [4] is strengthened by the precipitation of ε-copper phase, which is nearly pure copper. Reverted

0022–2461

austenite has been observed in this steel at ageing temperatures above 550 °C. This study assumed that the precipitation-hardening sequence is similar to those of Fe–Cu and Fe–Cu–X alloys [5–9]. Briefly, this involves the initial clustering of coherent copper-rich zones which later transforms to fcc ε-copper precipitate with further ageing. The above studies on the precipitation-hardening mechanism involving copper as the precipitate, conclude that the hardening phase has an fcc structure and is coherent with the bcc, low-carbon martensite.

The precipitation-hardening mechanism and the kinetics of ageing as well as aged microstructure of the 15-5 PH stainless steel has not been studied in detail. It is known that the fast kinetics of ageing in marage steels is due to the high defect density of martensitic matrix [10–13]. The studies listed above do not explain clearly the factors that affect the kinetics of ageing. The present study was concerned with the kinetics and the microstructure of the aged 15-5 PH stainless steel following laser melting, as well as after solution treatment.

Solidification of stainless steels has received a great deal of attention in the welding as well as casting literature [13–20]. It has been found that the most important parameter in preventing the so-called "hot cracking" in stainless steel weldments is the control over the composition as well as the solidification mode. Stainless steels that solidify in the primary austenite mode were found to be less resistant to hot cracking than the primary ferrite solidified alloys, due to extensive segregation of harmful elements (i.e. sulphur, phosphorus, niobium, silicon, etc.) to cell and solidification boundaries; these form low melting point eutectics. Primary-ferrite solidified welds, on the other hand, were found to be resistant to hot cracking due to higher solubility of these harmful elements in ferrite.

The results of fusion-zone microstructural characterization as well as a thermodynamic analysis of segregation of iron, nickel and chromium were reported in detail in a previous publication for laser welding of 15-5 PH stainless steel [21]. However, kinetics of ageing in the molten zone (henceforth called the fusion zone) is related to the structure and the laser processing parameters. Therefore, this study summarizes important aspects of the microstructure of the fusion zone with the main emphasis being on ageing structure and precipitation-hardening mechanism in the fusion zone and in the as-quenched alloy.

2. Experimental procedure

Laser-welding experiments were conducted on specimens of 15-5 PH whose composition is given in Table I, as supplied by the manufacturer. The alloys were in the as-quenched condition prior to laser welding. Austenizing treatment was carried out at 1040 °C before laser treatment as well as on the as-quenched samples. Following austenizing, specimens were quenched in water.

Autogenous laser welding was carried out with a 5 kW continuous wave CO_2 laser. The travel speed of the specimens was 4.3 mm s^{-1}. A 254 mm focusing lens was used. All welding experiments were made on samples of 25.4×25.4 mm^2 with a thickness of 11.2 mm under argon shielding gas.

After laser welding and ageing, specimens were sectioned and metallographic examinations were made on top and transverse sections. Final polishing was made with 0.06 μm alumina. Etching was conducted in a two-step procedure. First, the specimens were etched with Fry's reagent [22] and then dipped in Murakami's reagent for a few seconds until a good etching contrast was achieved.

The as-quenched and laser-welded samples were cut into the sizes of $\frac{1}{2}$ in $\times \frac{1}{2}$ in $\times \frac{1}{4}$ in (1 in $\simeq$ 2.54 cm) with a water-cooled saw. The surface oxide after laser welding was removed with 600 SiC paper prior to ageing. After this procedure, the specimens were aged in a liquid-lead bath at temperatures between 400 and 525 °C for 1–20 000 min. It was observed that liquid lead did not wet the samples. The heating rates of the samples to the required ageing temperatures were determined by embedding a chromel–alumel thermocouple into the centre of a sample of the same size. Ageing time was determined after the samples reached the respective ageing temperature. Temperature of the baths were controlled within $\pm$ 2 °C, with a chromel–alumel thermocouple shielded with stainless steel. The samples were quenched in water immediately after they were taken out of the liquid-lead bath.

Electron microscopy investigations were carried out on the as-quenched and on the precipitation hardened samples from the fusion zone and base metal. TEM samples were prepared by electropolishing in an electrolyte containing 10% perchloric acid and 90% acetic acid with a fischione jet polisher at room temperature, 50 V and 80 mA. These samples were then examined in a Jeol 100C electron microscope operated at 100 kV. A Leco 400 microhardness tester was used to determine the age-hardening response of both the base metal and the fusion zone. Hardness in the as-welded samples varied as a function of the location in the fusion zone. To be consistent in the age-hardening study, hardnesses in the fusion zone were recorded at a depth of 50 μm from the surface. Samples for age-hardening study of the fusion zone were prepared from the samples with welding speeds of 4.3 mm s^{-1}.

3. Results

Fig. 1 is a representative micrograph of the overall microstructure in the fusion zone. A microscopic examination of the welds revealed that they are free of hot cracks. Fig. 2 shows a higher magnification optical micrograph of the fusion zone where the solidification structure can be seen in detail. The dark-etched vermicular phase is primary ferrite which forms at the axes of the primary solidification cells. The roundish dark phase that is located at the cell boundaries (arrowed in Fig. 2) is eutectic ferrite which forms at the final stages of solidification.

The determination of the solidification path and characterization of the fusion zone was given in detail

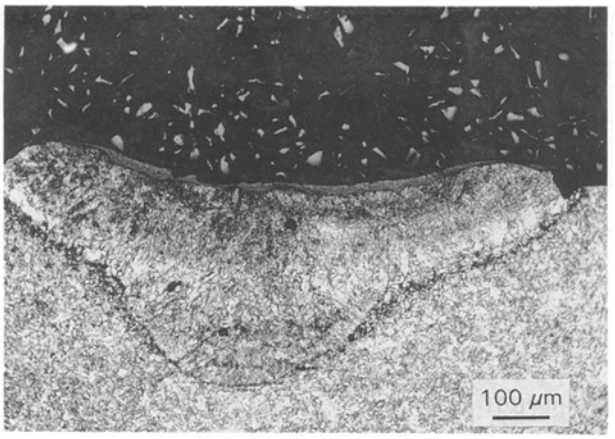

Figure 1 An optical micrograph of the fusion zone. Welding speed 3.4 mm s^{-1}.

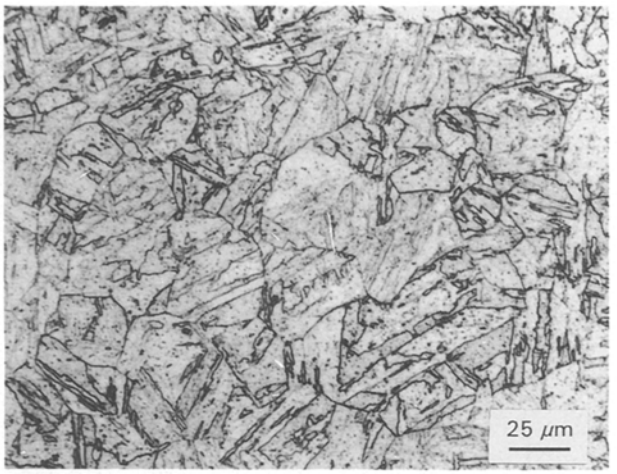

Figure 3 Optical micrograph of the as-quenched sample.

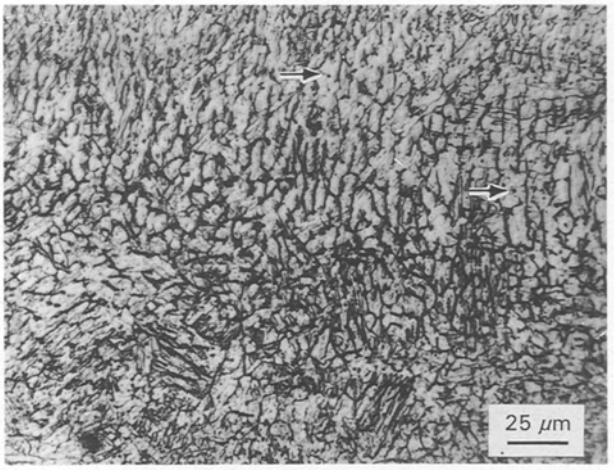

Figure 2 An enlarged section of Fig. 1 of the fusion zone. Eutectic delta ferrite is arrowed.

Figure 4 An electron micrograph of the as-quenched sample showing the lath martensitic structure prior to ageing.

in an earlier paper [21]. Therefore, a detailed description of the solidification structure will not be repeated here. However, it will be indicated briefly that the solidification mode was determined to be primary ferrite in the earlier work. Primary ferrite later transforms to austenite. The cores of the primary-ferrite cells are depleted in nickel. Owing to microsegregation at the solidification temperatures, the cores of the cells are "compositionally stabilized" ferrite, and this ferrite appears in a vermicular morphology. The rest of the primary-ferrite cell solidifies with the nominal composition until the final transient is reached where the final liquid to solidify reaches the composition of the eutectic and eutectic ferrite forms at the cell and solidification boundaries as evinced in Fig. 2. Austenite that forms from the primary ferrite as a result of diffusion-controlled decomposition transforms to martensite above room temperature. The M_s temperature of 15-5 PH was reported to be 203 °C [23].

Fig. 3 shows an optical micrograph of the as-quenched sample. This is also the starting microstructure prior to ageing. The prior austenite grain size is considerably larger than that of the fusion zone. This difference in the grain size has a major effect in the as-quenched hardness as will be discussed later. The microstructure of the fusion zone and the as-quenched material resemble a low-carbon lath martensite as shown in Fig. 4. Occasionally, some copper precipitates were found at the primary ferrite/prior austenite boundaries in the fusion zone.

The age-hardening curves for the fusion zone and the as-quenched material are shown in Figs 5 and 6. The initial hardness of the as-quenched samples were 350 VHN compared to 375 VHN of the fusion zone prior to ageing. The age-hardening curves are representative of any age-hardening alloy system. At low ageing temperatures, hardening is slow due to low diffusion rates and the maximum hardness is high due to the smaller and denser precipitates. At high ageing temperatures, hardness is lower because the critical nucleus size is large, and diffusion and, therefore, growth is faster. General observation in hardening characteristics of the fusion zone and the as-quenched material is such that the fusion zone has a higher hardness initially and at all ageing temperatures. This behaviour is summarized in Fig. 7 with the data of Figs 5 and 6. The reasons behind this mechanical behaviour are discussed in the following section.

Optical micrographs of the fusion zone and the base metal, after ageing at 400 °C for 1 h, are shown in

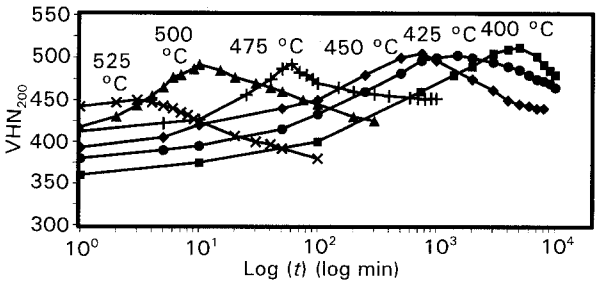

Figure 5 Hardness versus ageing time characteristics of the as-quenched base-metal samples at different temperatures.

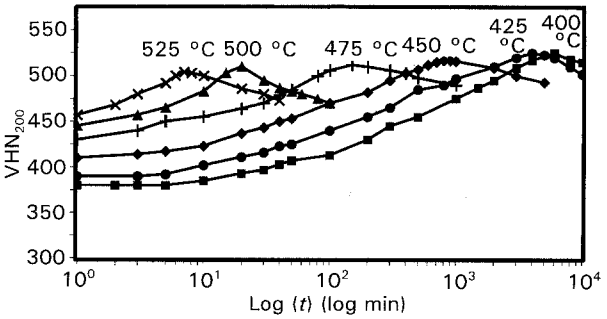

Figure 6 Hardness versus ageing time characteristics of the fusion zone at different ageing temperatures.

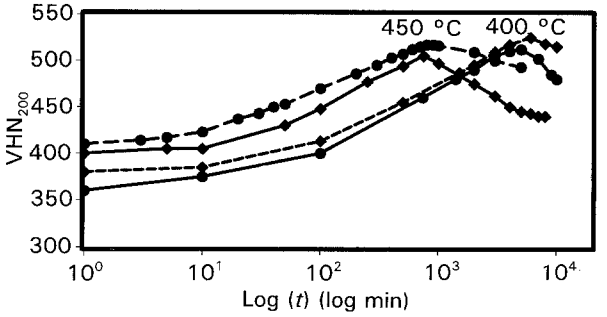

Figure 7 Comparison of hardness versus time characteristics of the (– – –) fusion zone and (——) base metal at 400 and 450 °C.

Figs 8 and 9, respectively. Finer cell size is also evident in the fusion zone in Fig. 9 when compared to the solution-treated and aged sample. The stable structure of the PH 15-5 at the ageing temperatures is austenite and therefore the metastable martensite is expected to transform to stable austenite. Decomposition is diffusion controlled and austenite is expected to nucleate at the grain boundaries in the as-quenched material and at the cell and solidification boundaries in the fusion zone. Two processes are expected to occur: recovery and recrystallization of the martensite, and nucleation and a diffusion-controlled growth of austenite into the bcc martensite. At the low ageing temperatures, i.e. at 400 °C, diffusion of substitutional elements are sluggish and austenite could not be observed (or austenite is very low in volume percentage). Electron micrographs at this stage revealed some precipitates in the bright-field images; however, no diffraction effects (i.e. extra spots or streaks) were found in the diffraction patterns, as shown in Figs 10 and 11. The low density and smaller size of precipitates are possible reasons behind this behaviour, as evidenced from the hardness versus time curve at this stage of ageing.

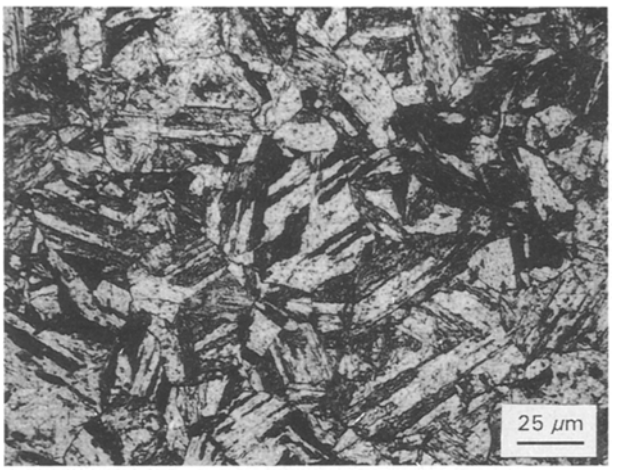

Figure 8 Optical micrograph of 15-5 PH after age-hardening at 400 °C for 1 h.

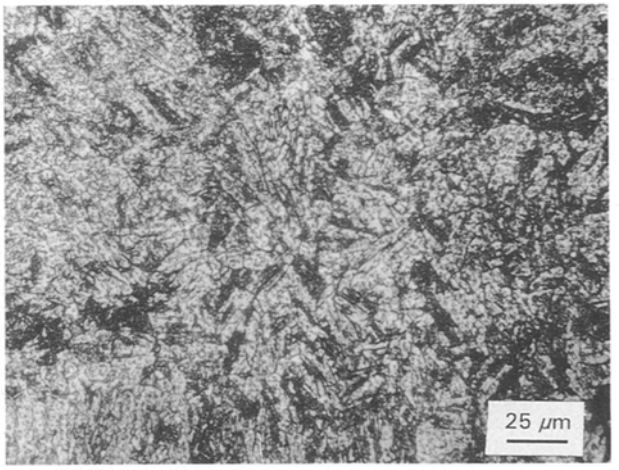

Figure 9 Optical micrograph of the fusion zone of 15-5 PH after age-hardening at 400 °C for 1 h.

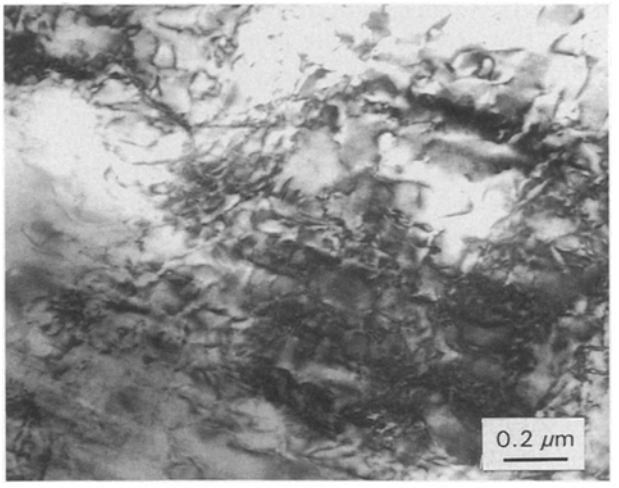

Figure 10 A bright-field image of the as-quenched 15-5 PH after age-hardening at 400 °C for 700 min.

Optical micrographs of the as-quenched sample after ageing at 500 °C for 7 min and 25 h are shown in

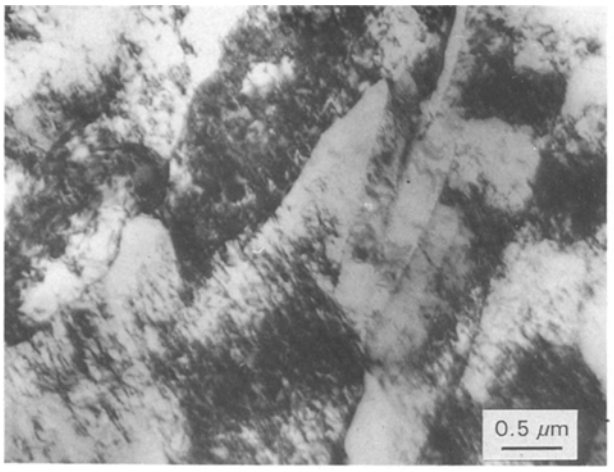

Figure 11 A bright-field image of the fusion zone 15-5 PH after age-hardening at 400 °C for 700 min.

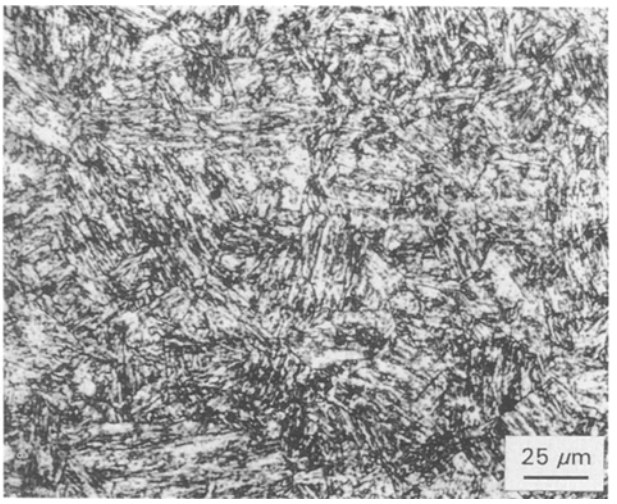

Figure 13 Optical micrograph of the as-quenched 15-5 PH after age-hardening at 500 °C for 25 h.

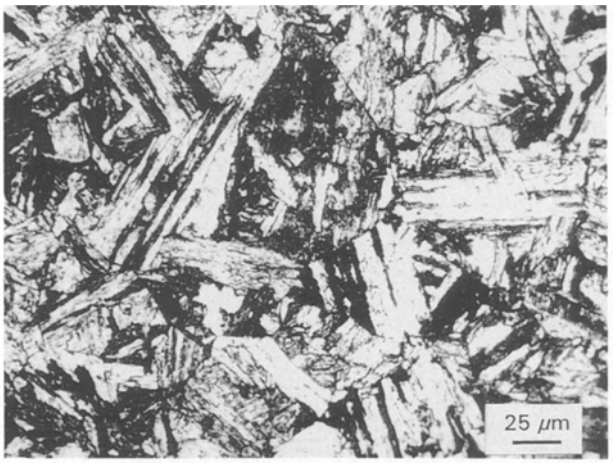

Figure 12 Optical micrograph of the as-quenched 15-5 PH after age-hardening at 500 °C for 7 min.

Figs 12 and 13. The short ageing times at this temperature do not reveal any macroscopic changes; however, recrystallization and transformation to austenite is evident in Fig. 13.

Electron micrographs of the as-quenched samples after ageing at 400 °C for 4000 min and 525 °C for 3 min are shown in Figs 14 and 15. At low ageing temperatures, more precipitates are observed on dislocations. Precipitates are both in the matrix and on the dislocations. Precipitation on the dislocations decreases as the ageing temperature increases, as shown in Fig. 15. Precipitates are identified as fcc ε-copper with a lattice parameter of 0.361 nm. At both ageing temperatures, the precipitates are found to be coherent with bcc martensite. The orientation relationship between the matrix and the precipitates is determined to be Kurdjumov–Sachs, i.e. $[0\,1\,1]_{fcc} \parallel [\bar{1}\,1\,1]_{bcc}$ and $(\bar{1}\,1\,1)_{fcc} \parallel [0\,1\,1]_{bcc}$.

An optical micrograph of the fusion zone after ageing at 500 °C for 3 min is shown in Fig. 16. The small cell size is obvious and it is much smaller than the grain size of the as-quenched material at the same ageing conditions (i.e. Fig. 12). Vermicular ferrite can be seen in the micrograph which has not decomposed to austenite at this stage of ageing. Electron micrographs of the fusion zone after ageing at 400 °C for 4000 min and 500 °C for 3 min are shown in Figs 17 and 18. The observations on the aged microstructures of the fusion zone are similar to that of as-quenched 15-5 PH. The precipitates are spherical fcc ε-copper and they are related to the bcc martensite with the Kurdjumov–Sachs relationship.

Final characterization of the aged structure is concluded with the identification of the phases in an overaged sample. The stable phase is austenite and is visible in the dark-field images and spherical copper precipitates are grown to a larger size. Both of these, i.e. transformation to austenite and growth of the precipitates, are responsible for the decrease in hardness. Both phases are shown in bright- and dark-field images in Fig. 19. Austenite nucleates at the lath or prior austenite boundaries and are located at these regions in the micrograph.

4. Discussion

The age-hardening curves obtained in the form of isothermal heat treatments of 15-5 PH stainless steel are similar to the age-hardening curves obtained in precipitation-hardening studies of substitutionally alloyed metals. General observations for the hardening in the fusion zone and in the as-quenched samples are such that they are similar. Generally, the fusion zone received slightly higher hardnesses than the as-quenched samples. Hardness curves of the fusion zone also indicate that the amount of the copper removed from primary ferrite during solidification due to microsegregation or evaporation is small.

The orientation relationship observed in this study is Kurdjumov–Sachs between ε-copper and the bcc matrix, which is common in fcc/bcc systems. The orientation relationship found in this study is also consistent with the orientation relationships obtained in Fe–6%Ni–2%Cu [24] and Fe–0.5%C–2%Cu [25] alloys. The Kurdjumov–Sachs relationship has been observed at all ageing temperatures except in the early ageing stages where no diffraction effects were

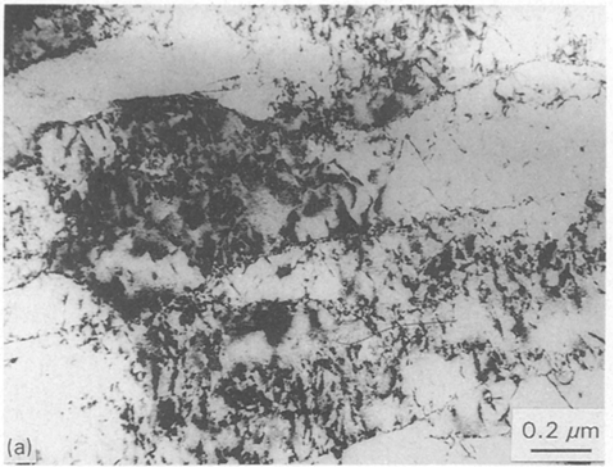

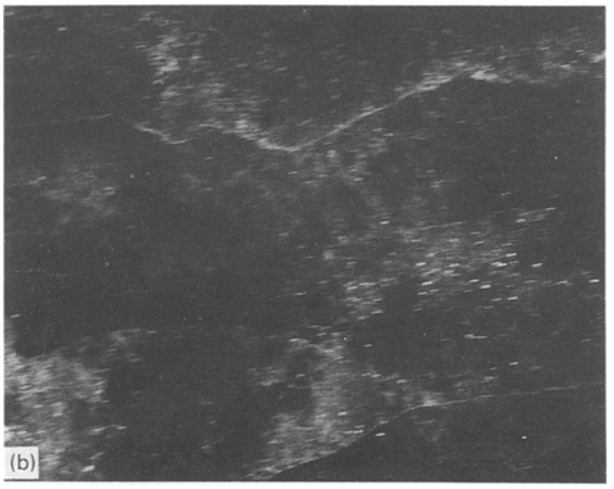

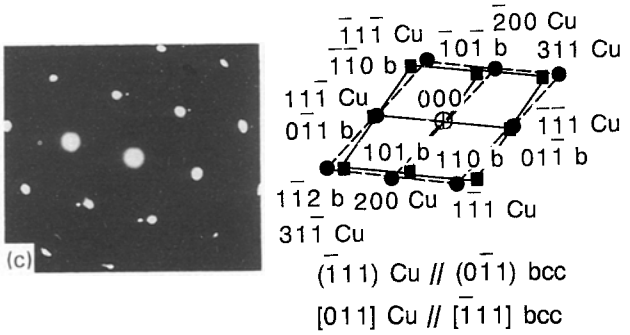

Figure 14 (a) Bright-field (b) dark-field and (c) diffraction pattern of base metal after ageing for 4000 min at 400 °C. The precipitates are identified as fcc copper being coherent with the bcc matrix. Some precipitates are observed on dislocations. (●) $[\bar{1}11]$ bcc, (■) [011] Cu.

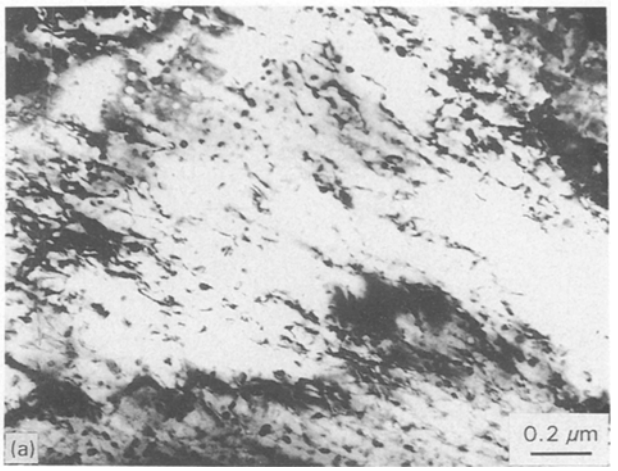

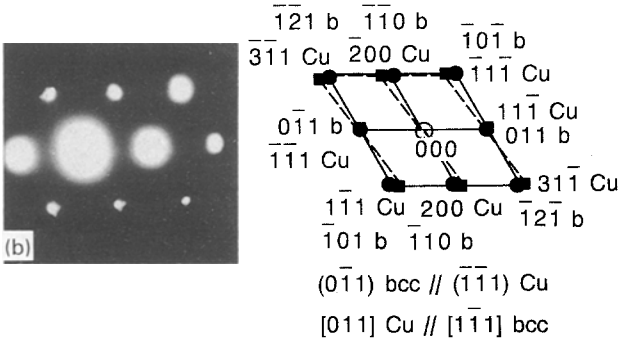

Figure 15 A transmission electron micrograph of base metal after ageing at 525 °C for 3 min. (a) Bright-field image and (b) diffraction pattern. Precipitates are fcc copper and they are coherent with the bcc matrix. (●) $[\bar{1}11]$ bcc, (■) [011] Cu.

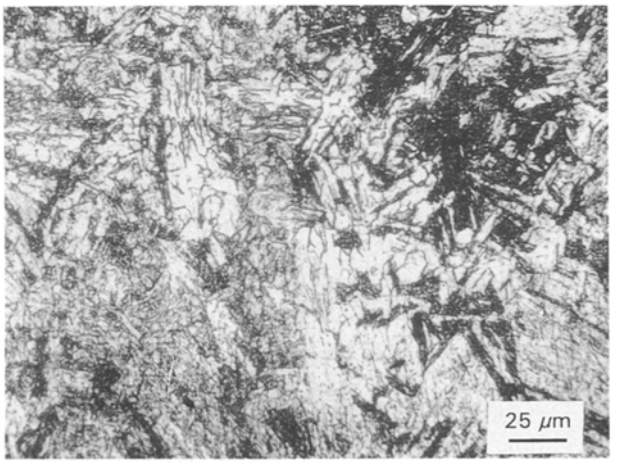

Figure 16 Optical micrograph of the fusion zone of 15-5 PH after age-hardening at 500 °C for 3 min.

detectable in the diffraction patterns: this is possibly due to the low density and small size of the precipitates. As the ageing time increased at a given ageing temperature, beyond the maximum hardness, associated hardness in both samples decreased. This behaviour is also consistent with theories where strengthening is assumed to be achieved by the interaction of dislocations with the coherency strain fields of precipitates. The decrease in the hardness is also partially related to the nucleation and growth of the stable-phase austenite.

To gain a further understanding of the mechanism of hardening and to investigate the different hardness levels at a given ageing temperature and time in the fusion zone and in the as-quenched samples, the kinetics and the rate-controlling factors should be determined. The temperature dependency of the kinetics of precipitation can be studied from an Arrhenius type equation, which is commonly obeyed in metals [12, 26]

$$\frac{1}{t_f} = A' \exp\left(\frac{-Q}{RT}\right) \quad (1)$$

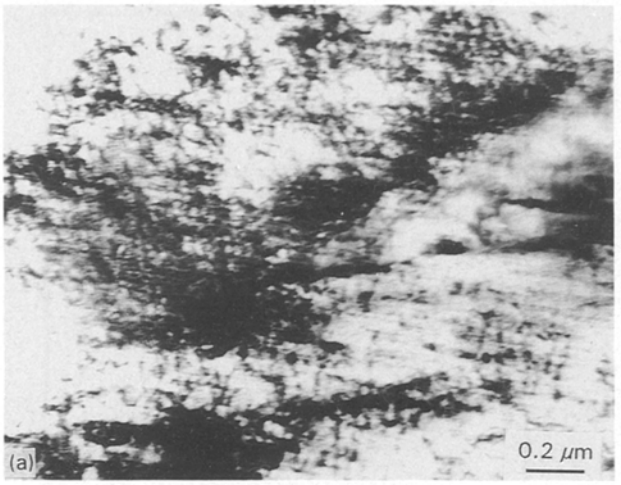

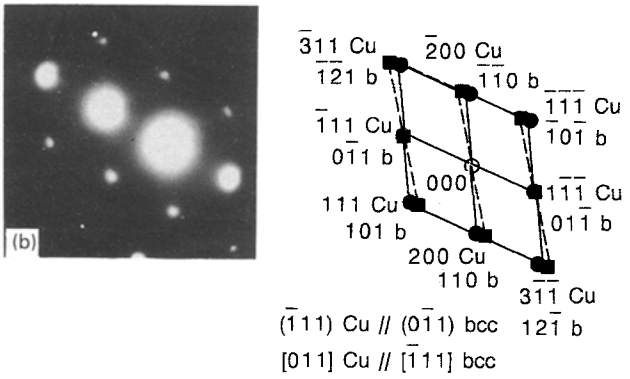

Figure 17 A transmission electron micrograph of the fusion zone after ageing at 400 °C for 4000 min. (a) Bright-field image and (b) diffraction pattern. (●) [0 1 1] Cu, (■) [1̄ 1 1] b c c.

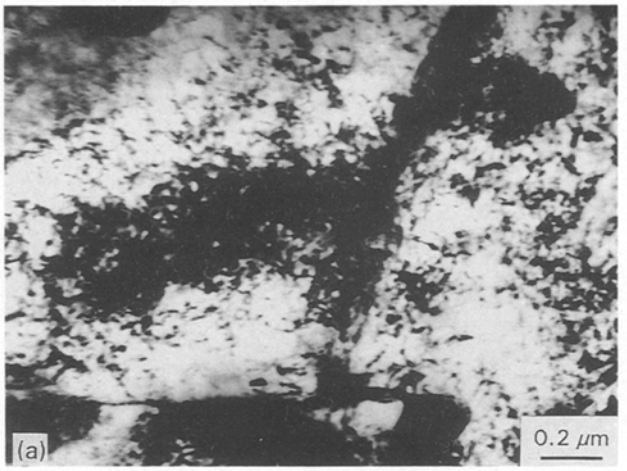

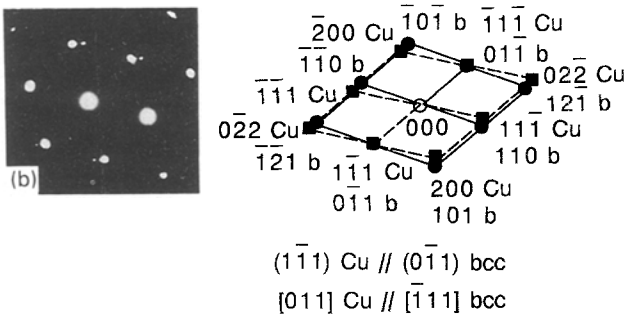

Figure 18 A transmission electron micrograph of the fusion zone after ageing at 525 °C for 3 min. (a) Bright-field image and (b) diffraction pattern. (■) [0 1 1] Cu, (●) [1̄ 1 1] b c c.

where t_f is the time to reach a certain fraction transformed, A' is a constant, R is the gas constant and T is the temperature (K). Equation 1 can be rewritten in terms of natural logarithms as

$$\ln(t_f) = A + \left(\frac{Q}{RT}\right) \qquad (2)$$

where $A = \ln 1/A'$. The slope of the $\ln(t_f)$ versus $1/T$ therefore gives the activation energy for the overall transformation. The activation energy determined in this manner is the sum of the activation energies for the overall process, i.e. nucleation and growth. It does not represent the activation energy for a single process such as nucleation or growth of precipitates. The usual assumption made in studies of ageing from Equation 2 is such that site saturation is assumed [26]. This means that nucleation occurs early in ageing or embryos are formed at the solution-treatment temperature or during quenching and therefore activation energy for nucleation can be neglected. Hence, the calculated activation energy can be compared to the activation energy for the diffusion of the strengthening element in the matrix.

Fig. 20 shows the $\ln(t_f)$ (time to reach a certain hardness) versus $1/T$ curves for the as-quenched samples. Generally, fusion zone and the as-quenched samples received lower peak hardnesses at high ageing temperatures (such as 525 °C), with respect to ageing at low temperatures. Therefore, some of the $\ln(t_f)$ versus $1/T$ curves are drawn for hardnesses lower than the peak hardness obtained by ageing at 525 °C. This is also a reasonable approach if the overlapping diffusion fields at lower temperatures are considered.

A basic understanding of the precipitation-hardening mechanism of 15-5 PH can be obtained through the calculation of the activation energy for the overall process combined with the microstructural characterization. This activation energy is calculated to be approximately 70 kcal mol^{-1} at high ageing temperatures (i.e. ageing above 450 °C), and 34 kcal mol^{-1} below this temperature through a least squares fit to the hardness data given in Figs 6 and 7. The same calculation was conducted for the samples from the fusion zone and the results are summarized in Fig. 21. The activation energy calculated in this manner is approximately the same for the fusion zone and for the as-quenched samples.

Observations of the same activation energies for the total strengthening imply that hardening mechanisms in both samples are the same. However, different activation energies obtained at low and at high temperatures imply that hardening mechanisms are different at low and at high temperatures for both structures. Factors that account for this behaviour are discussed below. The following discussion is based on the comparison of the calculated activation energies with activation energy for diffusion of copper in the b c c matrix.

The volume diffusion coefficient of copper in α-iron is [25]

$$D^{\alpha}_{Cu} = 8.6 \exp\left(\frac{-59.0}{RT}\right) \text{cm}^2\,\text{s}^{-1} \qquad (3)$$

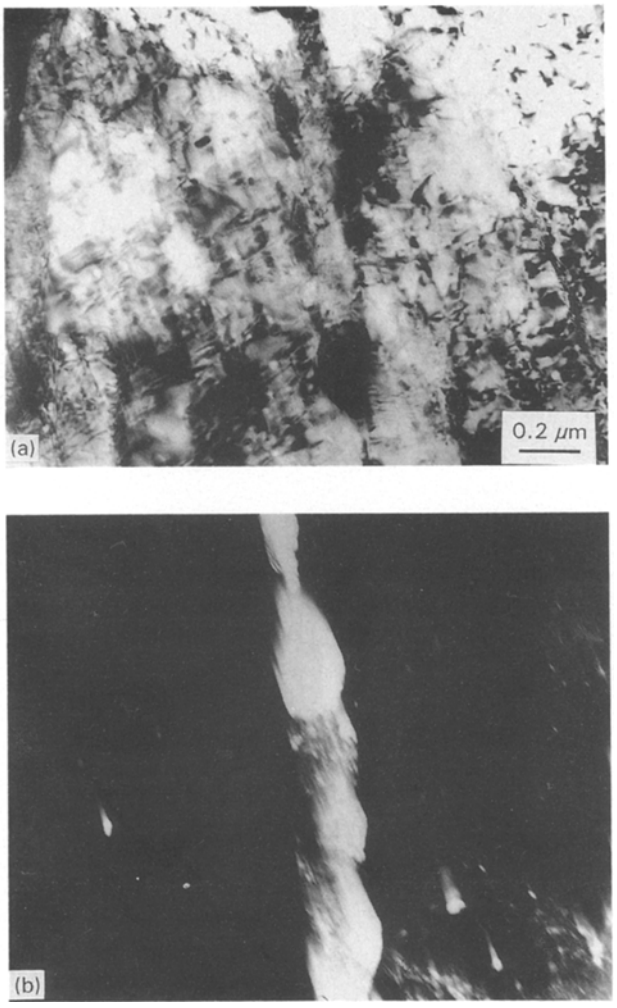

Figure 19 (a) Bright-field and (b) dark-field images of the base metal after overageing at 550 °C for 300 min.

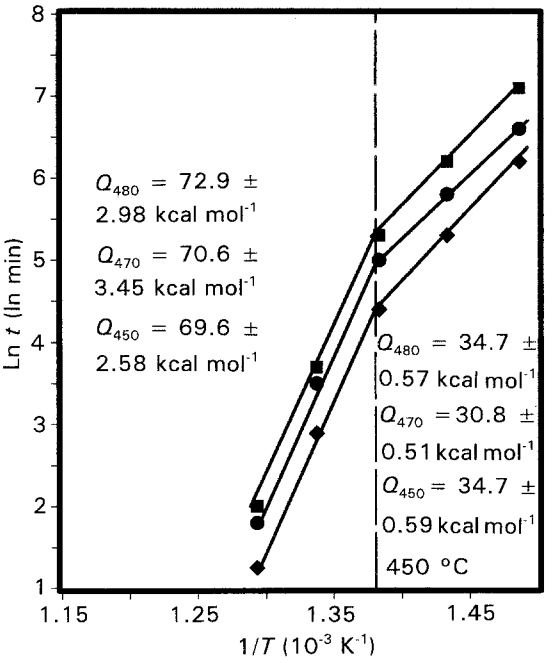

Figure 20 Arrhenius plot for precipitation in the base metal: (■) 480 VHN, (●) 470 VHN, (◆) 450 VHN.

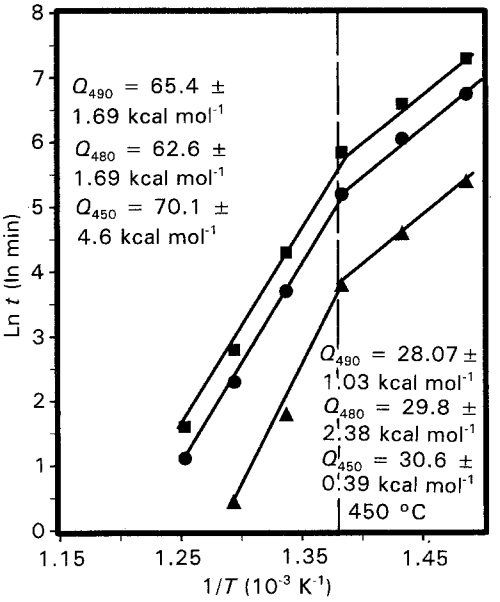

Figure 21 Arrhenius plot for precipitation in the fusion zone: (■) 490 VHN, (●) 480 VHN, (▲) 450 VHN.

As mentioned earlier, calculated activation energy from Equation 2 is the sum of the activation energies of nucleation and growth. It was assumed that the nuclei formed during solution treatment, during quenching or early in the ageing process. With this assumption, the calculated activation energy represents the activation energy for the growth because the activation energy for nucleation becomes zero.

The difference between the calculated activation energy and the activation energy for diffusion of copper in the bcc matrix can be explained in terms of activation energy for nucleation not being zero (i.e. the site-saturation assumption is not met), short-circuit diffusion, or the excess vacancy concentration from solution treatment or from liquid quenching. The high-temperature activation energy is discussed first.

The activation energy of 60–70 kcal mol^{-1} is approximately the same value for volume diffusion of copper in the bcc matrix. If this activation energy represents only the growth of the precipitates, the question arises of the benefits of the defect structure for the low-carbon martensite in enhancing the kinetics of precipitation. If, on the other hand, calculated activation energy represents that of short-circuit diffusion, it then also requires that the activation energy is the sum of the activation energies of nucleation and growth, because activation energy for short-circuit diffusion is approximately half of that of volume diffusion. However, as revealed by the hardness curves, there is no incubation period in hardening. Hardness increases as soon as the material is aged. The initial hardness at all ageing temperatures is always higher than the as-quenched hardness. Because an incubation period is not observed, the site-saturation assumption is met. Therefore, the calculated activation energy (60–70 kcal mol^{-1}) is the activation energy for growth. Hence, the slope of $\ln(t_f)$ versus $1/T$ curves represents the activation energy for growth of precipitates.

The activation energy calculated for the low-temperature part of ageing, i.e. below 450 °C, is one-half

the activation energy for diffusion of copper in the b c c matrix. It is known that short-circuit diffusion becomes important at temperatures below $\frac{1}{2}T_m$ [12]. At high temperatures, contribution of short-circuit diffusion to the total mass flow is low. As the temperature is lowered, short-circuit diffusion becomes important, depending on the grain size and dislocation density.

The calculated activation energy for precipitation at low ageing temperatures is consistent with short-circuit diffusion, mainly pipe diffusion through highly dislocated martensite. Low-carbon lath martensite of 15-5 PH has a high dislocation density, approximately 10^{12} cm^{-2} as well as a high population of low-angle lath boundaries which can be treated as arrays of edge dislocations. It is obvious that this defect structure enhances the mass transport of copper to feed the precipitates at low ageing temperatures. This calculated activation energy indicates that mass transport of copper is through the short-circuit diffusion channels and occurs mainly by pipe diffusion.

In summary, the activation energy for hardening at higher temperatures indicates that precipitation is controlled by diffusion of copper in the b c c lattice. At low temperatures, some precipitates were observed at the boundaries and on the dislocations (Fig. 14). This also supports the activation energy calculations and indicates that copper is fed to the precipitates through the dislocations. On the other hand, at high temperatures, precipitation was usually in the matrix. This observation is consistent with that of Hornbogen and Glen [27], who studied the precipitation of ε-copper in b c c ferrite in Fe–Cu alloys. The growth of ε-copper was found to be controlled by volume diffusion of copper in the heavily dislocated ferrite (quenched from 1000 °C). The lowest ageing temperature in their study was 500 °C.

Although the activation energies of the fusion zone and the as-quenched sample are approximately the same, the fusion zone was harder than the as-quenched sample at all ageing temperatures studied. Factors that may account for this behaviour can be given as follows: the activation energy for substitutional diffusion is affected by the defect density as well as by the concentration of vacancies. Because the fusion zone is quenched from liquid, one might expect an increase in the number of vacancies. This would initially increase the kinetics of ageing. However, vacancy diffusion is several orders of magnitude faster than substitutional diffusion; therefore, it is possible that these species diffused to the nearest sinks early in the ageing or during quenching from solidification temperatures. Within the experimental limitations of this work, there is no confirmation of excess vacancies in the fusion zone. Both the fusion zone and the as-quenched samples reach the peak hardness at the same ageing temperature. Similar activation energies for hardening also indicate that precipitation kinetics are the same, and microstructural characterization confirms this.

The above discussion leaves the grain size and the finer structure as the major factors for the higher hardness obtained in the fusion zone. After a certain ageing time, the martensitic structure in both samples are broken down due to recovery and recrystallization; and from that point on strength is controlled by the size and the density of the precipitates, as well as prior austenite grain size.

The fusion zone had a finer structure composed of two phases (martensite and ferrite) to start with, and a higher hardness (375 VHN compared to 350 VHN) prior to ageing, than the as-quenched samples. Therefore, this is possibly the main reason for its higher hardness. Smaller grain size may also affect the total mass flow of copper to the precipitates through the larger grain-boundary area and hence lead to early strengthening. However, this is not reflected in the calculated activation energies. It has been shown that marage steels obey a Hall–Petch relation in terms of grain-size strengthening, both in the aged and in the as-quenched conditions [28]. Therefore, the above discussion on the slightly higher hardness of the fusion zone being due to the grain size is more appropriate than the assumption of the presence of an excess vacancy concentration.

5. Conclusions

Hardening was found to be fast in both structures and no incubation period was observed in the hardness versus time curves at any of the ageing temperatures. The precipitates were found to be mostly spherical in both samples. This indicates that the strain-energy barrier for nucleation is negligible and the shape of the precipitates were controlled by the surface-energy requirements. Precipitates are coherent with the matrix at all ageing temperatures and they are related to the b c c martensite with a Kurdjumov–Sachs relationship.

The hardening mechanism in both samples is the same. This is due to the fact that activation energies calculated for the low- and high-temperature ageing are approximately the same. At high temperatures, growth of the precipitates is controlled by the mass transport of copper in the b c c martensite. At low temperatures, the contribution of pipe diffusion to the apparent diffusivity increases.

The higher hardness found in the fusion zone is the result of smaller grain size. Because the fusion zone is cooled from solidification temperatures, prior austenite grain size is smaller than the as-quenched sample. This high hardness of the fusion zone is also consistent with the grain-size dependency of strengthening of marage steels.

The conclusions may be summarized as follows.

1. Precipitation of ε-copper is the main reason for the strengthening of 15-5 PH in the fusion zone and in the base metal. ε-copper is related to the b c c martensite with a Kurdjumov–Sachs orientation relationship and is coherent with the matrix.

2. The mechanism of strengthening is similar in the fusion zone and in the base metal. Activation energies calculated for strengthening are approximately the same for both samples.

3. The higher activation energy at higher ageing temperatures indicates that hardening is controlled by

the volume diffusion of copper in the bcc matrix. At lower temperatures, the activation energy for precipitation is low, i.e. contribution of the high dislocation density to the apparent diffusivity is large. The growth of precipitates is, therefore, controlled by the mass transport of copper through short-circuit diffusion.

4. The fusion zone has a higher hardness prior to ageing and at all ageing temperatures. This is due to finer grain structure resulting from rapid solidification. During age-hardening, lath martensitic structures of both samples are broken down after a certain period of ageing. From that point on, strength is controlled by the size and density of the precipitates as well as the grain size.

5. Transformation of the martensite to austenite starts at the later stages of ageing. Austenite nucleates at the boundaries and grows into the martensite lath packs and, together with overageing, is responsible for softening.

Acknowledgements

Partial support for this study was acquired from Sandia National Laboratory, Albuquerque NM, under contract SANDIA 23-7498 and is gratefully acknowledged. The authors also thank Dr E. S. Metin for helpful discussions.

References

1. S. DING, D. JUANG and J. W. MORRIS, *Met. Trans.* **7A** (1976) 637.
2. D. PECKNER and I. M. BERNSTEIN, "Handbook of Stainless Steels" (McGraw-Hill, 1977) p. 72.
3. W. A. SPITZIG, J. M. CHILTON and C. J. BATON, *Trans. ASM.* **1968** (1968) 299.
4. U. K. VISVANATHAN, S. BANERJEC and R. KRISNAN, *Mater. Sci. Eng.* **A 104** (1988) 181.
5. E. HORNBOGEN, *Acta Metall.* **10** (1962) 525.
6. S. R. GOODMAN, S. S. BRENNER and T. R. LOW Jr, *Met. Trans.* **4** (1973) 2371.
7. G. R. SPEICH and R. A. ORIANI, *TMS-AIME* **233** (1965) 623.
8. S. K. LAHIR, D. CHANDRA, L. H. SCHWARTZ and M. E. FINE, *ibid.* **245** (1969) 1865.
9. E. RASANEN, *Scand. J. Metall.* **2** (1975) 257.
10. D. T. PETERS and C. R. CUPP, *TMS-AIME* **236** (1966) 1420.
11. H. J. RACK and D. KALISH, *Met. Trans.* **5** (1974) 1595.
12. J. W. CHRISTIAN, "Transformations in Metals and Alloys", Part 1 (Pergamon Press) p. 544.
13. J. C. LIPPOLD and W. F. SAVAGE, *Weld. J.* **58** (1979) 266.
14. *Idem, ibid.* **59** (1980) 48.
15. *Idem, ibid.* **61** (1982) 388.
16. M. J. CIESLAK, A. M. RITTER and W. F. SAVAGE, *ibid.* **61** (1982) 1.
17. M. J. CIESLAK and W. F. SAVAGE, *ibid.* **59** (1980) 136.
18. J. A. BROOKS, J. C. WILLIAMS and A. W. THOMPSON, *Met. Trans.* **14A** (1983) 23.
19. A. M. RITTER, M. J. CIESLAK and W. F. SAVAGE, *ibid.* **14A** (1983) 37.
20. S. A. DAVID, *Weld. J.* **60** (1981) 63.
21. K. OZBAYSAL and O. T. INAL, *Mater. Sci. Eng.* **A 130** (1990) 205.
22. "Metals Handbook", Vol. 8, 8th Edn (ASM Metals Park, OH) p. 98.
23. "Precipitation Hardening Stainless Steels" (Republic Steel Publ., 1973) p. 6.
24. R. A. RICKS, P. R. HOWELL and R. W. K. HONEYCOMBE, *Met. Trans.* **10A** (1979) 1049.
25. J. A. WASYNCZCUK, PhD Thesis, Berkeley (1986).
26. K. BURKE, "Kinetics of Phase Transformations in Metals" (Pergamon Press, 1965) p. 115.
27. E. HORNBOGEN and R. C. GLENN, *TMS-AIME* **218** (1960) 1064.
28. H. J. RACK, *Mater. Sci. Eng.* **34** (1978) 263.

Received 20 August 1992
and accepted 27 September 1993